https://doi.org/10.5194/egusphere-2026-746
Preprint. Discussion started: 16 February 2026

Global and diurnal variations in tropospheric ammonia observed from a constellation of hyperspectral infrared sounders in three different LEO orbits

Jiancong Hua[1], Runyi Zhou[1], Mengya Sheng[1], Zhao-Cheng Zeng[1]

[1]School of Earth and Space Sciences, Peking University, Beijing 100087, China

Correspondence to: Zhao-Cheng Zeng (zczeng@pku.edu.cn)

Abstract. As a reactive nitrogen compound, atmospheric ammonia (NH_3) plays a key role in the global nitrogen cycle. Tracking the spatiotemporal dynamics of NH_3 is crucial to quantify its emissions and depositions, as well as offering insights to inform the regulation of anthropogenic emission sources. Currently, the diurnal cycle of NH_3 remains under-constrained, particularly in regions lacking geostationary satellite observations, which poses a challenge to accurate emission quantification. To address this gap, we construct an integrated constellation to achieve quasi-geostationary-like global monitoring coverage, comprising China's FengYun-3 (FY-3) series satellites and the Cross-track Infrared Sounder (CrIS). FY-3E operates in a dawn-dusk orbit with equatorial overpassing time at 05:30 am/pm, while FY-3F operates in a mid-morning orbit with overpassing time at 10:00 am/pm. Both are equipped with the second-generation High Spectral Infrared Atmospheric Sounder (HIRAS-II). CrIS, operating with overpassing time at 01:30 am/pm, provides supplementary observations in an afternoon orbit. In this study, hyperspectral infrared observations from the constellation are utilized to retrieve global NH_3 columns based on the optimal estimation method. Six maps of global NH_3 for every 4-hour in each day are retrieved. The retrieval results in four weeks of different seasons in 2024, as a demonstration, show elevated columns in global major source regions, including Western Europe, North America, North China Plain and North India. In addition, the diurnal and seasonal cycles of NH_3 over these regions using all observations in 2024 are also investigated. The constellation reasonably captures the diurnal (every 4-hour) and seasonal cycles of NH_3 columns, effectively mitigating the constraints in regions without geostationary observations. Consistency of the retrievals among different satellites is demonstrated by comparing with geostationary observations from the Geostationary Interferometric Infrared Sounder (GIIRS). The sensitivity of NH_3 detection in the lower atmosphere as quantified by the column averaging kernel (AVK) from the retrieval shows diurnal variations that dependent on thermal contrast, defined as the temperature difference between the surface and the lower atmospheric layer. This study demonstrates the capability of the integrated constellation, comprising FY-3E/HIRAS-II (dawn-dusk), FY-3F/HIRAS-II (mid-morning), and CrIS (afternoon), to monitor global and diurnal NH_3 variations at unprecedentedly six distinct times of a day, and has the potential to enhance the global climate-monitoring capacity of polar-orbiting meteorological satellites.

https://doi.org/10.5194/egusphere-2026-746
Preprint. Discussion started: 16 February 2026

1 Introduction

As a critical reactive nitrogen compound, ammonia (NH_3) holds considerable importance in the atmosphere and global nitrogen cycle, yet it also acts as a hazardous pollutant affecting human health and ecosystems. Specifically, it contributes to smog via its neutralization of sulfuric and nitric acids, resulting in the generation of secondary aerosols including ammonium sulfate and ammonium nitrate. (Galloway et al., 2004; Behera et al., 2013). These particles can travel long distances, degrading air quality and disrupting ecological balance (Erisman et al., 2013). These ammonium-based particles, along with NH_3 itself, can be converted into various reactive nitrogen forms that trigger acid precipitation, eutrophication, and reduced biodiversity (Sutton et al., 2011). Under specific conditions, ammonium nitrate particles may volatilize to reform gaseous NH_3, creating a dynamic cycle that complicates its environmental impacts (Weber et al., 2016; Guo et al., 2018). Agriculture serves as the dominant source, stemming from fertilizer storage, livestock manure, and the application of mineral nitrogen fertilizers to crops (Fowler et al., 2013). Secondary contributors to NH_3 emissions encompass biomass combustion, industrial operations, and automobiles fitted with three-way catalytic converters. (Galloway et al., 2003; Dammers et al., 2017). After being emitted into the atmosphere, NH_3 exhibits a brief residence time ranging from several hours to a handful of days, and its primary removal pathways are dry and wet deposition processes (Liu et al., 2013; Dammers et al., 2017; Zhang et al., 2018). These deposition processes accelerate soil acidification, further exacerbating the ecological damage. Beyond air quality and ecosystem impacts, the aerosols derived from NH_3 also influence climate by scattering solar radiation, modifying albedo, and altering the properties of clouds (Adams et al., 2001; Abbatt et al., 2006; Isaksen et al., 2009; Myhre et al., 2013).

Different technologies have been used to monitor atmospheric NH_3. A number of in situ monitoring sites equipped with Fourier transform infrared (FTIR) spectrometers have been established (Jiménez et al., 2015; De Mazière et al., 2018). Moreover, satellites furnished with high-resolution infrared spectrometers have provided unprecedented spatiotemporal sampling of global NH_3 distributions, and this has driven major progress in understanding NH_3 emission and deposition fluxes covering spatial scopes ranging from local-level to global-scale, together with their temporal fluctuation characteristics. Polar-orbiting satellites are capable of delivering global observational coverage up to two times per day, including the Infrared Atmospheric Sounding Interferometers (IASI, e.g., Clarisse et al., 2009) at 09:30/21:30 (Local Solar Time, LST), Tropospheric Emission Spectrometer (TES, e.g., Beer et al., 2008; Shephard et al., 2011), the Atmospheric Infrared Sounder (AIRS, e.g., Warner et al., 2016)) and the Cross-track Infrared Sounder (CrIS, e.g., Shephard and Cady-Pereira, 2015) at 01:30/13:30 LST, the Thermal and Near-infrared Spectrometer for Observation-Fourier Transform Spectrometer (TANSO-FTS; e.g., Someya et al., 2020) at 01:00/13:00 LST and FengYun-3D (FY-3D, e.g. Zhou et al., 2024) at 02:00/14:00 LST. Recently, diurnal variations of atmospheric NH_3 over the Asian region have been observed using the Geostationary Interferometric Infrared Sounder (GIIRS) aboard the FengYun-4A (FY-4A/GIIRS, Clarisse et al., 2021) and FengYun-4B (FY-4B/GIIRS, Zeng et al., 2023; Sheng et al., 2025) satellites. In addition, the IRS on the Meteosat Third Generation satellite (IRS/MTG) which was launched in 2025 observes NH_3 over Europe and Africa (Holmlund et al., 2021). Such geostationary orbit-based monitoring offers significant advantages and potential for investigating NH_3 diurnal variations, which in turn facilitates a deeper

https://doi.org/10.5194/egusphere-2026-746
Preprint. Discussion started: 16 February 2026

understanding of its emission, deposition, transport and other related processes. However, the lack of geostationary orbit observations across most global regions especially in the Southern Hemisphere prevents multiple daily observations from being achieved. Atmospheric NH_3 shows notable spatiotemporal variability, largely attributed to its primary emission characteristics and short atmospheric lifetime. This inherent variability underscores the urgent need for a high-resolution and globally comprehensive monitoring system.

To address this gap, we construct an integrated constellation to achieve quasi-geostationary-like global monitoring coverage, comprising China's FengYun-3 (FY-3) series satellites and CrIS. FY-3E operates featuring an equatorial overpass time of 05:30 am/pm local solar time (LST), while FY-3F operates in a mid-morning orbit with overpassing time at 10:00 am/pm. Both satellites carry the second-generation High Spectral Infrared Atmospheric Sounder (HIRAS-II) onboard. CrIS, operating with overpassing time at 01:30 am/pm, provides supplementary observations in an afternoon orbit. Similar constellation has been developed for monitoring volcanic sulfur dioxide (Zeng et al., 2025). NH_3 retrievals employing the optimal estimation method, will be conducted under this framework to enable quasi-geostationary observations up to six times a day globally. This work is expected to provide crucial observational data for clarifying global and diurnal NH_3 variations.

The subsequent sections of this paper are organized as follows. Section 2 elaborates on the methodological approaches adopted in the present research. Section 3 showcases the retrieval results from the constellation, while section 4 is the discussions. Finally, the conclusions are drawn in section 5.

2 Methodologies

2.1 A constellation of hyperspectral infrared sounders

The High Spectral Infrared Atmospheric Sounder (HIRAS) aboard the FY-3 satellite series is a Fourier Transform Michelson interferometer. It detects upwelling infrared radiative signals across the short-wave, mid-wave, and long-wave infrared bands. HIRAS-II is the second-generation of the HIRAS sensor and is installed on both FY-3E and FY-3F, which were successfully launched in 2021 and 2023, respectively (Zhang et al., 2022a, b). FY-3E/HIRAS-II is deployed in a dawn-dusk orbit, with an equatorial overpass time of 05:30 am/pm (Local Solar Time, LST), while FY-3F/HIRAS-II operates in a mid-morning orbit featuring an overpass time of 10:00 am/pm LST. Combined with CrIS aboard the Joint Polar Satellite System-1 (JPSS-1) platform, which has an overpass time of 01:30 am/pm LST, these three sensors form a global constellation observation system (Fig. 1a). Their overpass times are shown in Fig. 1b, and the corresponding histograms are presented in Fig. 1c.

Both HIRAS-II instruments aboard the FY-3E and FY-3F satellites, as well as the CrIS share key technical specifications with a nadir spatial resolution of 14 km and an unapodised spectral resolution of 0.625 cm^{-1} (Zhang et al., 2024). Specifically, HIRAS-II provides continuous spectral coverage across 650–2550 cm^{-1} via 3041 channels, while CrIS matches this spectral resolution, ensuring all three instruments fully cover the characteristic rotational-vibrational ν_2 band of NH_3 centered near 10.5 μm. For NH_3 retrieval, we focus on the 955–975 cm^{-1} spectral window extracted from observations of all three instruments. Critically, their performance across this NH_3 absorption band is highly consistent. We randomly selected one day of

https://doi.org/10.5194/egusphere-2026-746
Preprint. Discussion started: 16 February 2026

observations from the three satellites over the North China Plain and calculated their spectral noise. The noise equivalent differential temperature (NedT) of HIRAS-II aboard FY-3E and FY-3F is approximately 0.08 K, while that of CrIS is around 0.05 K. These noise levels are of a comparable magnitude and sufficiently sensitive to detect variations in NH_3, ensuring uniform observational quality for cross-instrument analysis (Zavyalov et al., 2013; Shephard and Cady-Pereira, 2015; Zhang et al., 2024). While CrIS already has well-established and mature NH_3 products from the CrIS Fast Physical Retrieval (CFPR) dataset developed by Environment and Climate Change Canada (Shephard et al., 2020), we adopt a unified retrieval algorithm for all three instruments. This choice is driven by the need to ensure consistency across the satellite constellation, enabling direct inter-comparability between FY-3E/HIRAS-II, FY-3F/HIRAS-II, and CrIS observations. For CrIS retrievals, we use JPSS-1 CrIS Level 1B Full Spectral Resolution V3 data as input, maintaining methodological coherence with our processing of HIRAS-II observations.

https://doi.org/10.5194/egusphere-2026-746
Preprint. Discussion started: 16 February 2026

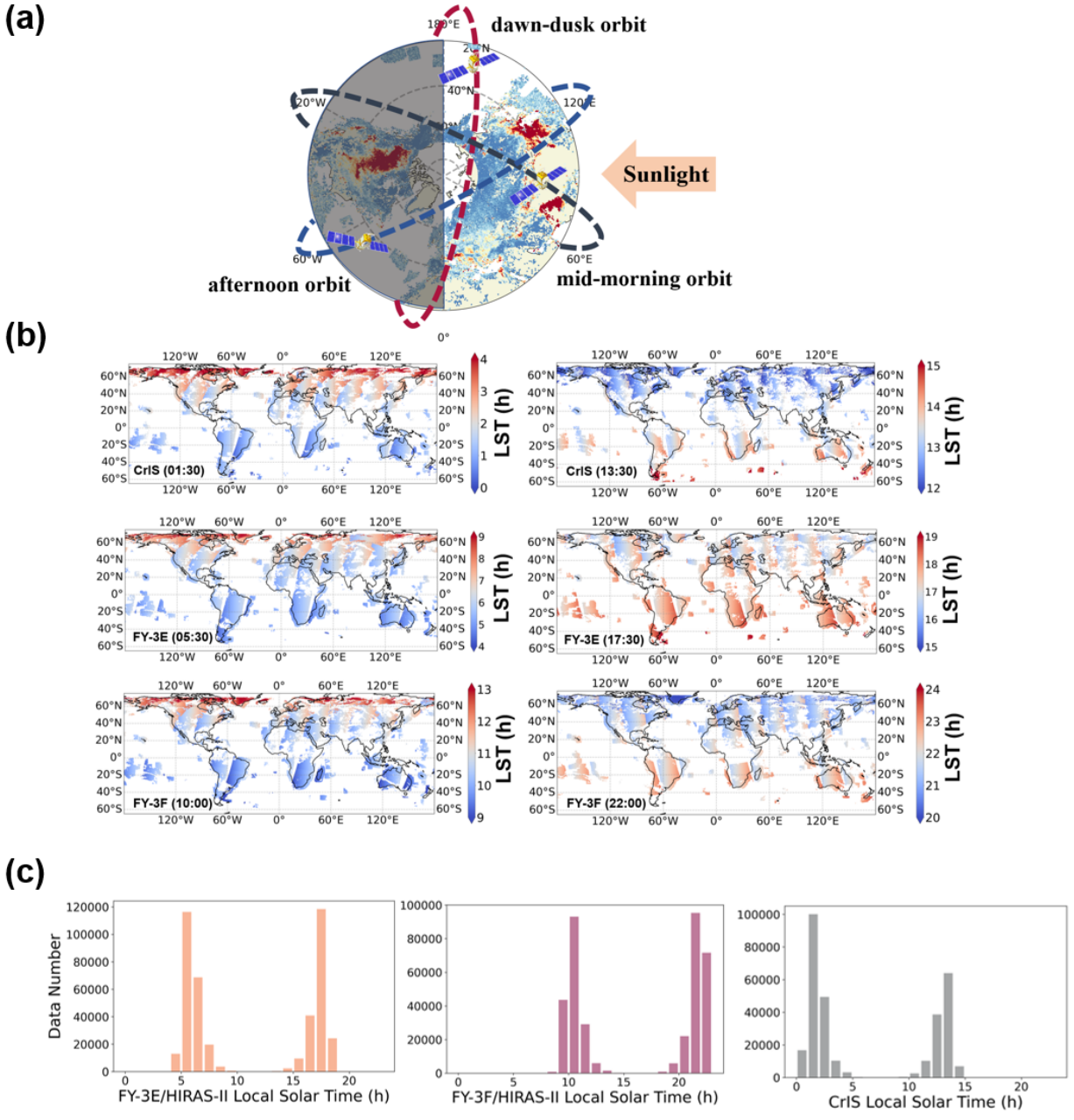

Figure 1. (a) Schematic diagram of three polar-orbiting satellites with different orbits. FY-3E/HIRAS-II operates in a dawn-dusk orbit, with an equatorial overpass time of 05:30 am/pm LST, FY-3F/HIRAS-II is in a mid-morning orbit with an equatorial overpass time of 10:00 am/pm LST, and the CrIS has an equatorial overpass time of 01:30 am/pm LST. The color gradient in the background represents the retrieved global distribution of NH_3 total columns on 19 July 2024, as will be discussed in subsequent analyses. (b) Local Solar Time (LST) of observations acquired by FY-3E/HIRAS-II, FY-3F/HIRAS-II and CrIS over terrestrial and offshore regions. Observations over polar areas and remote oceans are excluded. These maps are constructed from cloud-screened observations collected on 19 July, 2024. (c) Histograms of the overpass Local Solar Time (LST) for FY-3E/HIRAS-II, FY-3F/HIRAS-II, and CrIS. Examples are derived from observations taken on 19 July, 2024.

https://doi.org/10.5194/egusphere-2026-746
Preprint. Discussion started: 16 February 2026

2.2 Optimal estimation methods

For the retrieval, only cloud-screened spectra from FY-3E, FY-3F, and CrIS are used. To eliminate cloudy pixels and ensure data consistency across sensors, we implement a unified cloud filter based on empirical relationships between the European Centre for Medium-Range Weather Forecasts Reanalysis v5 (ERA5) water vapor column, and the difference between ERA5 surface temperature and the satellite-observed brightness temperature at 900 cm^{-1} (Wells et al., 2020, 2022). A consistent optimal estimation framework serves as the fundamental basis for retrievals from all three satellites. Our approach builds on the FengYun-Low Earth Orbit Atmospheric Infrared Retrieval (FY-LeoAIR) algorithm, first designed for trace gas retrievals from FY-3E/HIRAS-II measurements (Zeng, 2025; Zeng et al., 2025; Hua et al., 2025). FY-LeoAIR adapts the FY-GeoAIR algorithm, initially created for the FY-4B/GIIRS instrument (Zeng et al., 2023), with targeted refinements to suit operational characteristics of the three platforms and an expansion from the Asia-focused region to a global coverage. FY-LeoAIR has been successfully utilized for the retrieval of CO and VOCs from FY-3E/HIRAS-II observations (e.g., Zeng, 2025; Hua et al., 2025). While FY-LeoAIR shares similar retrieval framework with FY-GeoAIR, we introduce a key modification for this study. A profile scaling approach is used to retrieve a single scale factor applied to a fixed a priori NH_3 profile. The weak spectral signature of NH_3, which has a signal degree of freedom mostly below 1, cannot robustly constrain layer-by-layer variations in the profile. This differs from the full-profile retrieval approach in Zeng et al., (2023). Profile scaling offers greater computational efficiency for global applications, as it avoids estimating partial columns for each atmospheric layer. Because NH_3 is most abundant in the lower atmosphere, our retrieval focuses on 11 atmospheric layers extending from the surface to the 200 hPa level. A fixed a priori profile instead of a variable one is adopted, so that any spatiotemporal changes in retrieved NH_3 column concentrations reflect only information from satellite observations, rather than variations in the prior. The detailed description of the construction of the forward model and inverse model and the model inputs can be referred to Zeng et al. (2023).

In short, FY-LeoAIR combines a clear-sky infrared radiative transfer forward model with an optimal estimation-based inverse model. An optimal state vector for minimizing discrepancies between forward model-simulated spectra and sensor-measured spectra is derived by the optimal estimation framework. In practice, the retrieval algorithm outputs the state vector that minimizes the cost function defined as:

$$J(\boldsymbol{x}) = \chi^2 = [\boldsymbol{y} - \mathbf{F}(\boldsymbol{x}, \boldsymbol{b})]^T \boldsymbol{S_\varepsilon}^{-1} [\boldsymbol{y} - \mathbf{F}(\boldsymbol{x}, \boldsymbol{b})] + (\boldsymbol{x} - \boldsymbol{x_a})^T \boldsymbol{S_a}^{-1} (\boldsymbol{x} - \boldsymbol{x_a}) , \quad (1)$$

Here, $\boldsymbol{y}$ denotes the satellites measured radiance within the NH_3 retrieval window. $\mathbf{F}$ is the forward model that produces simulated radiance for the retrieval process. $\boldsymbol{x}$ represents the state vector comprised of scale factors for gas profiles. $\boldsymbol{x_a}$ denotes the a priori vector. $\boldsymbol{b}$ stands for a set of fixed non-retrieved auxiliary parameters. $\boldsymbol{S_a}$ is the a priori covariance matrix corresponding to the state vector. $\boldsymbol{S_\varepsilon}$ represents the measurement error covariance matrix, treated as a diagonal matrix derived from spectral noise estimates. Retrieval outputs include the NH_3 column, posteriori column retrieval uncertainty estimation, and column averaging kernel (AVK). The column AVK quantitatively represents the response of total NH_3 column to

https://doi.org/10.5194/egusphere-2026-746
Preprint. Discussion started: 16 February 2026

variations in the partial column at each layer, which is important for cross-comparison and model assimilation of satellite retrievals.

3 Results and Discussions

3.1 Global variations of NH_3 columns from the LEO constellation

We analyze the retrieval results for four one-week periods representing different seasons of 2024, specifically January 12–18, April 12–18, July 17–23, and October 1–7. We first retrieve global daily maps of NH_3 column, then re-grid all maps to a 0.5° × 0.5° spatial resolution and conduct a seven-day average for each seasonal period. A strict quality control process is applied to ensure the reliability of satellites retrievals. Observations that fail to achieve convergence within 10 iterations are excluded from the dataset. We then implement a series of post-filters, retaining only those retrieval results that satisfy all the following criteria simultaneously. First, the retrieved NH_3 columns are required to be positive. Second, the absolute difference in surface skin temperature between the a priori and retrieved values is less than 10 K. Third, the retrieval error of the column does not exceed 300%. Fourth, the surface AVK is greater than 0.1. Fifth, the thermal contrast (TC), defined as the temperature difference between the surface and the lowest atmospheric layer, is larger than 3 K. Sixth, a threshold for surface emissivity at 8.3 μm is set at 0.9, with only results meeting this threshold retain; this step is designed to avoid the occurrence of abnormally high NH_3 column concentrations over desert regions, consistent with the method of Clarisse et al. (2019). The surface emissivity data used for this filter are obtained from the Combined ASTER and MODIS Emissivity over Land Database Monthly Global 0.05° V003, which provides global monthly emissivity data at a 0.5° spatial resolution.

As shown in Figs. 2 and 3, seasonal variations in global NH_3 columns are evident across the four study periods. In January, elevated NH_3 columns are concentrated in North India and Central Africa, which is primarily associated with ongoing agricultural activities such as winter fertilizer application and extensive biomass burning for land clearance in these regions. In April, high NH_3 loading persists in North India, East China and Central Africa, driven by intensified spring planting and corresponding fertilizer use in agricultural hotspots. Southeast Asia also exhibits increased NH_3 levels during this month, a pattern attributed to widespread slash-and-burn agriculture practices that are common in the regional dry season to prepare farmland. Additionally, scattered high NH_3 columns are observed in parts of North America, likely linked to localized agricultural operations and small-scale biomass burning. In July, high NH_3 columns remain concentrated in North India, North China, Central Africa and Western Europe. The sustained high levels in these areas correlate with summer agricultural activities and elevated temperatures that enhance emissions (Ding et al., 2024). In particular, large-scale wildfires prevalent in summer North America exert a broad-range impact, leading to significantly elevated NH_3 columns across extensive regions as a result of biomass burning releasing substantial amounts of NH_3. Within the smoke plumes, rapid gas-particle partitioning of NH_3 and favorable ammonium nitrate formation in cold, high-altitude conditions sustain column enhancements even as the plume disperses, reinforcing the widespread NH_3 elevations we observe (Lindaas et al., 2021). October still sees detectable high NH_3 columns over North India, where post-harvest agricultural residues burning and late-season fertilizer application

https://doi.org/10.5194/egusphere-2026-746
Preprint. Discussion started: 16 February 2026

maintain elevated emissions. In South America, elevated NH_3 levels are mostly attributed to combined effects of fertilizer
180 usage for autumn crops and biomass burning, as documented by Luo et al. (2022). The seasonal patterns reflect the close linkage between NH_3 distribution and region-specific anthropogenic activities, alongside seasonal natural processes. These spatial patterns exhibit general consistency with results from IASI (e.g., Van Damme et al., 2015) and CrIS (e.g., Shephard et al., 2020).

https://doi.org/10.5194/egusphere-2026-746
Preprint. Discussion started: 16 February 2026

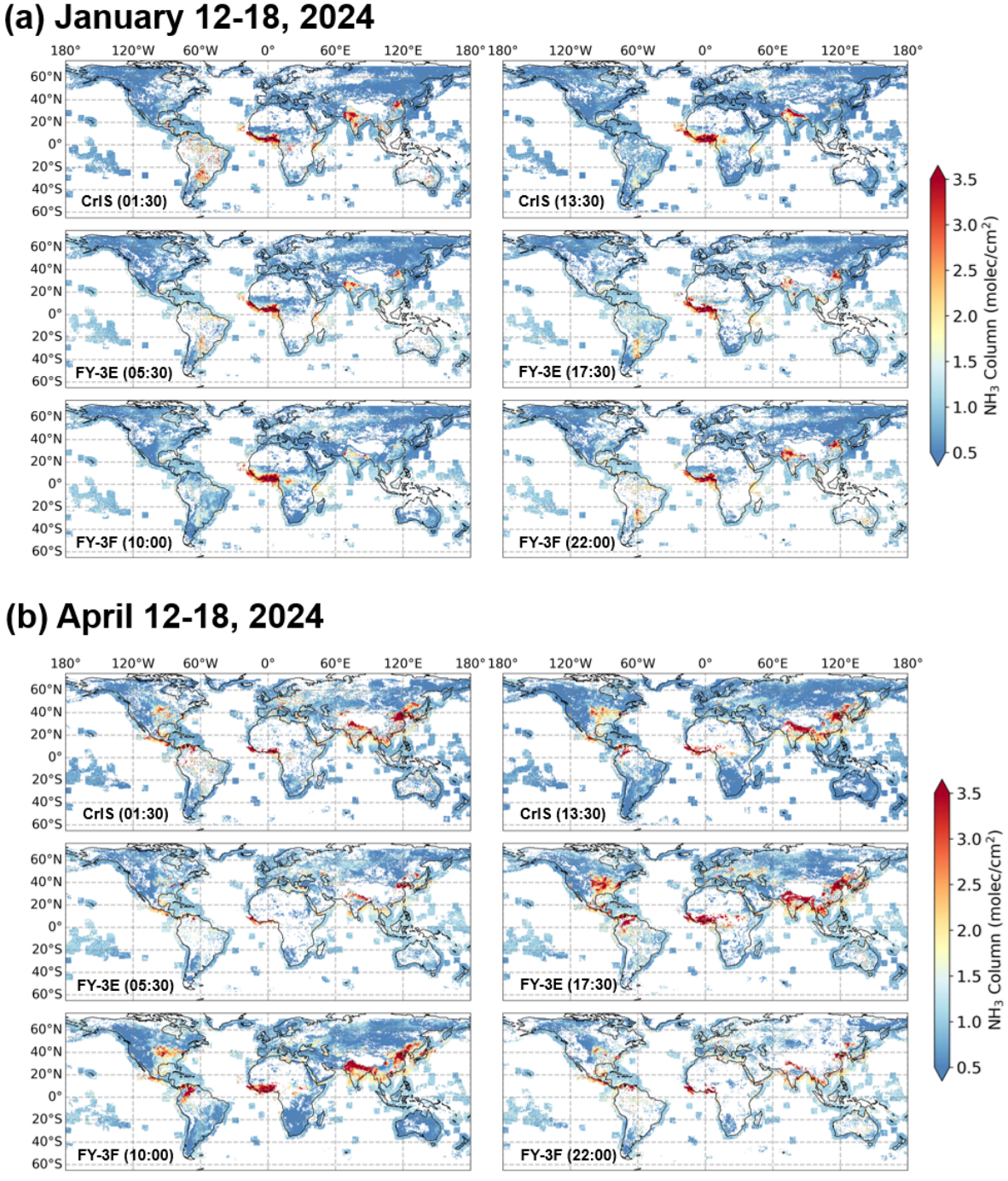

Figure 2. Seven-day mean NH_3 total columns retrieved from FY-3E, FY-3F, and CrIS for six different time slots, gridded to a 0.5° × 0.5° spatial resolution. The data correspond to the period of (a) January 12–18, 2024 and (b) April 12–18, 2024.

https://doi.org/10.5194/egusphere-2026-746
Preprint. Discussion started: 16 February 2026

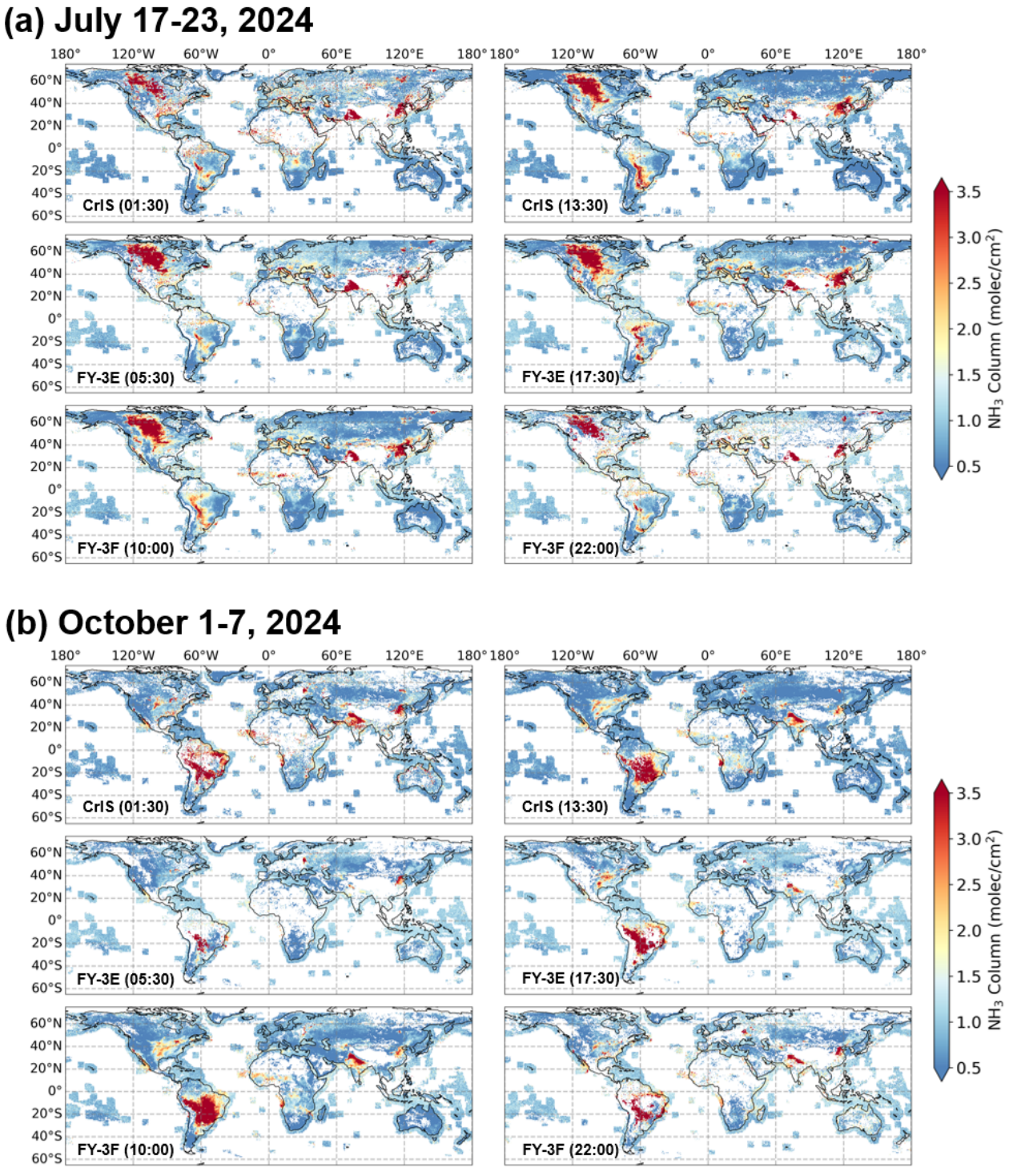

Figure 3. Same as Fig. 2, but for the period of (a) July 17–23, 2024 and (b) October 1-7, 2024.

https://doi.org/10.5194/egusphere-2026-746
Preprint. Discussion started: 16 February 2026

3.2 NH_3 variations in global major source regions from the LEO constellation

To conduct in-depth analysis of NH_3 variations, we select three major emission hotspots, locating inside the North China Plain (118°E, 37°N), the Indo-Gangetic Plain (78°E, 28°N), and Central United States (100.5°W, 36.5°N), respectively. These hotspots are characterized by intensive agricultural activities and high livestock densities, consistent with the high-emission areas for their substantial NH_3 column abundances and distinct diurnal and seasonal dynamics. For each hotspot, we extract data within a 2.5° × 2.5° grid centered at the specified coordinates, covering six overpass times per day. Monthly averages are calculated, with valid data defined as having more than 10 effective observation points to ensure statistical robustness. TC affects the retrieval accuracy (Bauduin et al., 2017) and that higher TC contributes to better retrievals (Clarisse et al., 2010). To ensure high quality NH_3 columns retrievals, we implement stringent quality control measures. An observation is used only if TC exceeds 5 K, and the surface AVK, which reflects the information content of observations related to near-surface NH_3, surpasses 0.3 to guarantee reliable capture of surface variation. These filtering strategies enhance the credibility of diurnal and spatial variation analyses for the three key regions.

The diurnal cycles of retrieved NH_3 columns for the three hotspots are presented in Fig. 4, with IASI retrievals overlaid for comparison. Also shown are the monthly mean planetary boundary layer (PBL) heights from ERA5 reanalysis. All three hotspots exhibit consistent seasonal differences in diurnal variability, a pattern that consists with Clarisse et al.'s (2021) findings from GIIRS observations and aligns with broader research on NH_3 dynamics (Tevlin et al., 2017). Warmer months (April–September) show distinct day-night contrasts, while winter months (December–February) display minimal diurnal fluctuations.

For the North China Plain (Fig. 4a), FY-3E, FY-3F, CrIS, and IASI data collectively reveal that warm-season NH_3 columns follow a clear diurnal pattern with a peak between 10:00 and 13:30 local solar time (LST), and nighttime values approximately 50–60% lower than daytime maxima. The peak corresponds to intensified agricultural activities (e.g., fertilization and livestock management) and temperature-driven volatilization from soils and animal waste, mechanisms identified by Ernst and Massey (1960) and Sutton et al. (2013) as primary drivers of daytime NH_3 emission enhancement. Higher PBL height during the day facilitates vertical diffusion of NH_3 and contributes to the observed column dynamics Saylor et al. (2010). In contrast, winter NH_3 columns over the North China Plain show negligible diurnal variation, which is probably due to the fact that cold-season emissions are limited by low temperatures and reduced agricultural activity (Kuang et al., 2020; Clarisse et al., 2021).

The Indo-Gangetic Plain (Fig. 4b) exhibits the highest overall NH_3 columns among the three hotspots, with warm-season daytime columns nearly double those of the North China Plain. This regional difference stems from higher concentrations of NO_x and SO_2 (Clarisse et al., 2021; Ding et al., 2024) over the North China Plain that act as neutralizing agents, shortening the lifetime of atmospheric NH_3 (Liu et al., 2018; Wang et al., 2020). The most pronounced warm-season diurnal amplitude appear in the Indo-Gangetic Plain, with daytime columns up to three times higher than nighttime values.

https://doi.org/10.5194/egusphere-2026-746
Preprint. Discussion started: 16 February 2026

This pattern reflects the region's intensive irrigated agriculture, high livestock density (Perrone, 2020), and the exponential dependence of NH_3 emissions on temperature (Hempel et al., 2016). Winter diurnal variations here are similarly weak, though NH_3 columns remain higher than those in the other two regions due to persistent agricultural activity in milder winter conditions (Saraswati et al., 2018).

For the Central U.S. (Fig. 4c), the diurnal variation pattern is broadly consistent with the Asian regions but with a smaller amplitude. Warm-season NH_3 columns peak between LST 11:00 and 14:00, with daytime values approximately 1.5–2 times higher than nighttime levels, while winter columns show little diurnal fluctuation. This consistency supports that temperature, PBL dynamics, and diurnal emission sources (e.g., agricultural activities) are universal drivers of NH_3 diurnal cycles across high-emission regions globally, which is evidenced by Saylor et al. (2010) from their analysis of NH_3 measurements in the southeastern U.S.. The smaller amplitude compared to the Indo-Gangetic Plain likely reflects moderate temperature variations and balanced NH_3 emission and deposition processes, as reported by Warner et al. (2017) in satellite observations of North American agricultural regions. Li et al. (2025) further emphasize that local deposition in vegetation-dense areas offsets large-scale transport, explaining the muted diurnal amplitude relative to Asian regions.

The spatial and seasonal dynamics of NH_3 columns are further illustrated in Figs. 5–7 for the North China Plain, Indo-Gangetic Plain, Central U.S., respectively, retrieved by FY-3E/HIRAS-II, FY-3F/HIRAS-II and CrIS. Fig. A1 further illustrates monthly mean NH_3 columns variations for these three regions, confirming consistent time series across the six daily satellite overpasses and coherent seasonal trends. All three regions exhibit a consistent seasonal peak in NH_3 columns during spring to summer (March–August), with the lowest values in winter (December–February). For the North China Plain, all retrievals at six distinct times show that NH_3 columns peak in June, with spatial coverage expanding across the entire plain during warm months, reflecting widespread agricultural activities (e.g., wheat fertilization and livestock waste management) and favorable meteorological conditions for emission (Zhang et al., 2010; Zhan et al., 2021). In contrast, winter maps display sparse, localized high-NH_3 patches, consistent with reduced agricultural activity and lower temperature-driven volatilization (Schjoerring et al., 1998).

For the Indo-Gangetic Plain, Fig. 6 shows that the region maintains the highest NH_3 columns year-round, with spatial hotspots concentrated in the central plain during both day and night. However, daytime maps exhibit broader coverage extending to the plain's peripheries, while nighttime maps show more concentrated hotspots near emission sources. For the central U.S., Fig. 7 reveals the lowest overall NH_3 columns among the three regions, with daytime spatial patterns spreading across the Corn Belt and Great Plains, and nighttime patterns contracting to smaller agricultural clusters.

The comparison between daytime and nighttime spatial patterns underscores the critical role of PBL height in shaping NH_3 distribution. Daytime maps display broader spatial coverage because higher PBL height (typically 1–3 km during warm-season days) facilitates vertical and horizontal diffusion of NH_3 away from emission sources. In contrast, nighttime maps show more localized NH_3 columns, as lower PBL height (often <500 m at night) traps emissions near the surface (Walker et al.,

https://doi.org/10.5194/egusphere-2026-746
Preprint. Discussion started: 16 February 2026

2006; Wang et al., 2019). This pattern is especially pronounced over the North China Plain, where Figs. 5b-5d show contiguous high-NH_3 zones across the plain, while Fig. 5a, 5e and 5f limit high columns to central agricultural districts. For the Indo-Gangetic Plain, nighttime spatial maps also reveal persistent NH_3 in the residual layer, an effect linked to PBL collapse in the evening, which traps NH_3 at higher altitudes for several hours (Lonsdale et al., 2017; Kuang et al., 2020). This residual layer NH_3 explains why some nighttime retrievals show broader coverage than expected, even with low PBL height, and aligns with Clarisse et al. (2021)'s observation that NH_3 vertical profile assumptions can impact nighttime retrieval accuracy.

https://doi.org/10.5194/egusphere-2026-746
Preprint. Discussion started: 16 February 2026

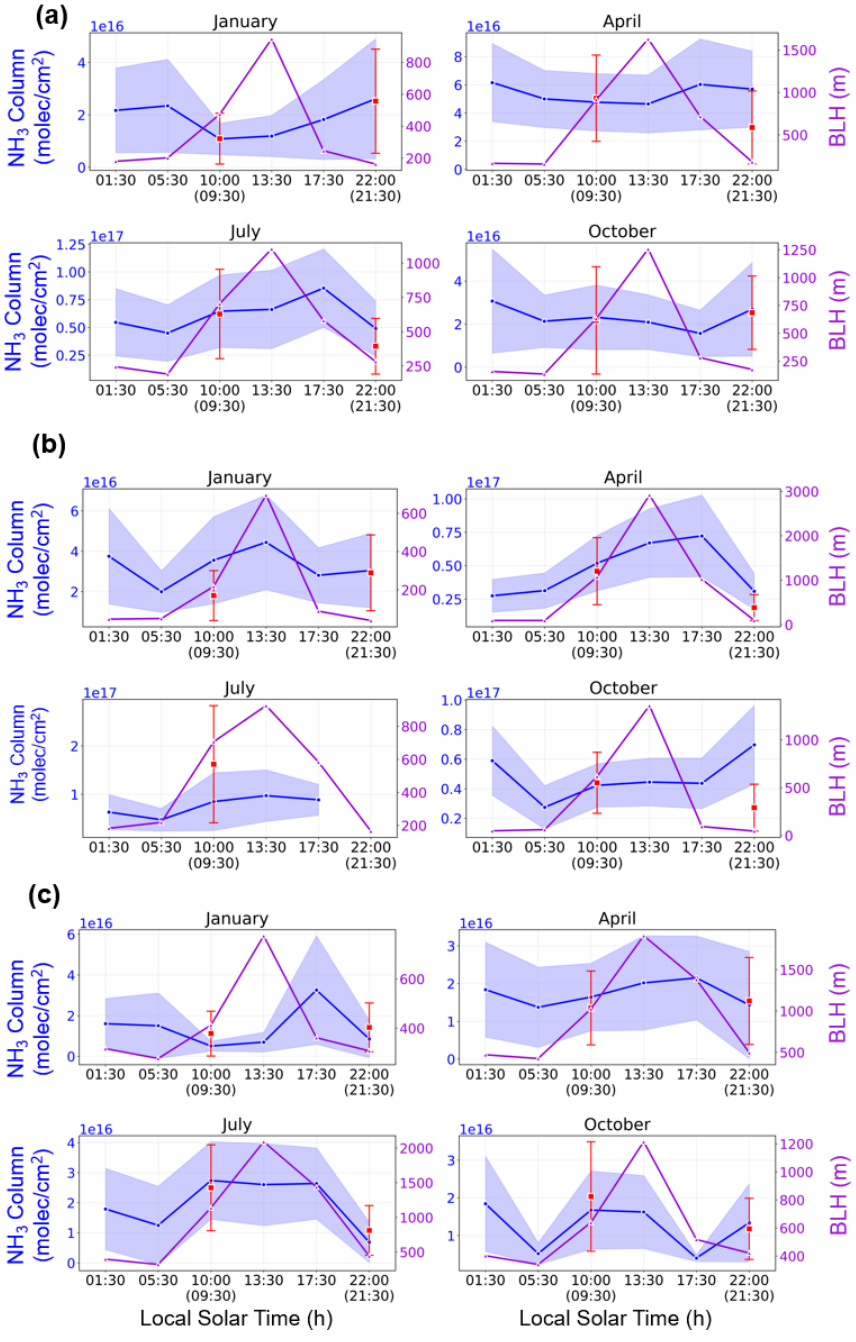

Figure 4. Diurnal cycles of retrieved NH_3 columns from FY-3E, FY-3F and CrIS over (a) the North China Plain (118°E, 37°N), (b) the Indo-Gangetic Plain (78°E, 28°N), and (c) Central U.S. (100.5°W, 36.5°N). The locations of these three sites are indicated in Figs. 5-7, respectively. Blue circles denote the mean values within the 2.5° × 2.5° grid, and the blue shaded area represents the standard deviation for each overpassing time. IASI retrieval results for the same region are overlaid for comparison: red squares indicate IASI mean values, with error bars representing their standard deviation. The time axis is expressed in Local Solar Time. The diurnal variation of monthly mean planetary boundary layer height (BLH) is also plotted in purple.

https://doi.org/10.5194/egusphere-2026-746
Preprint. Discussion started: 16 February 2026

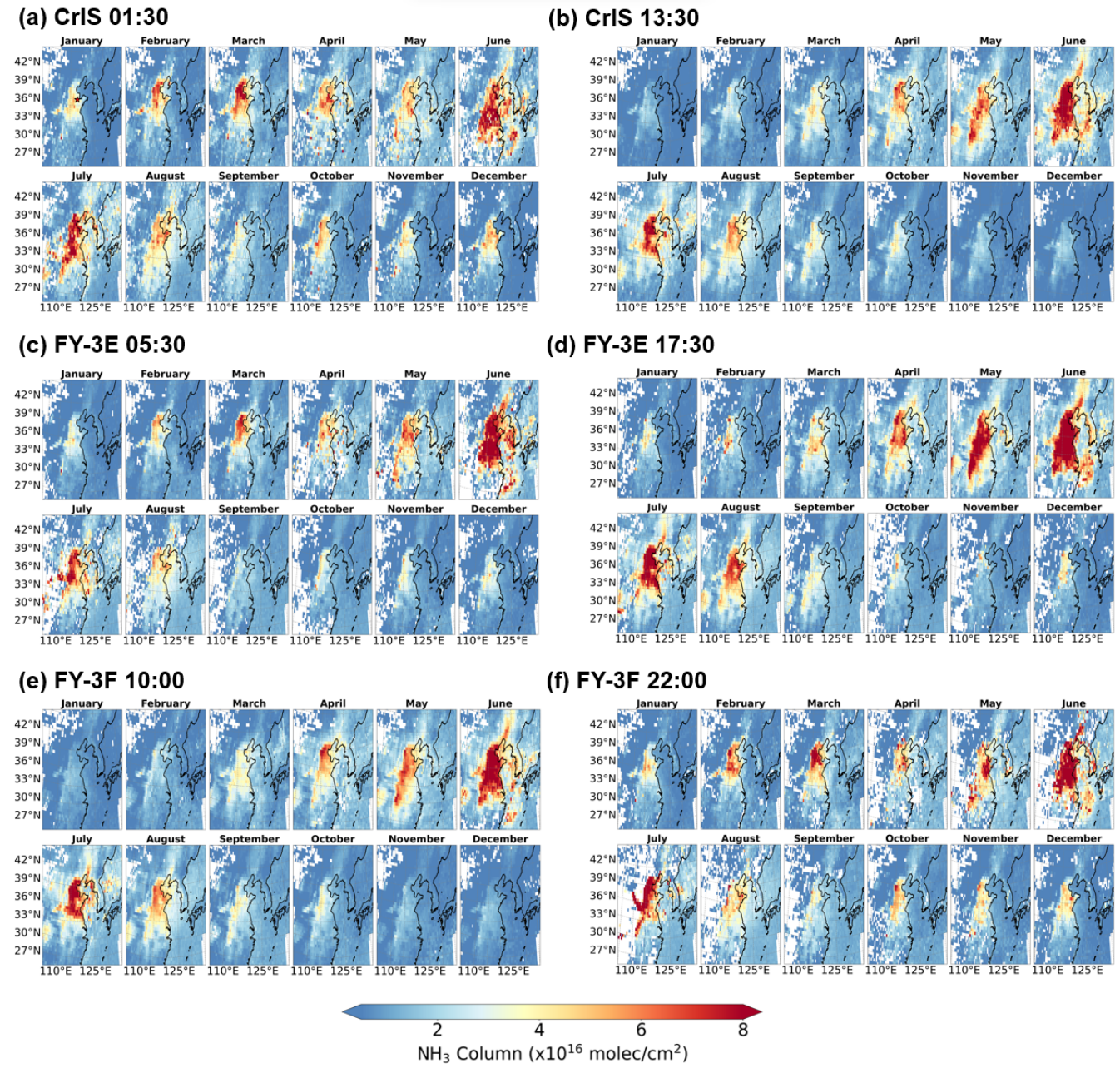

Figure 5. Monthly mean NH_3 total column (0.5° × 0.5° grid) over the North China Plain retrieved by (a) CrIS at night overpasses (01:30 LST), (b) CrIS at daytime overpasses (13:30 LST), (c) FY-3E/HIRAS-II at dawn overpasses (05:30 LST), (d) FY-3E/HIRAS-II at dusk overpasses (17:30 LST), (e) FY-3F/HIRAS-II at morning overpasses (10:00 LST), and (f) FY-3F/HIRAS-II at evening overpasses (22:00 LST), during 2024. The red star in the January panel of Fig. 5a indicates the location of the site (118°E, 37°N) analyzed in Figs. 4 and 8.

https://doi.org/10.5194/egusphere-2026-746
Preprint. Discussion started: 16 February 2026

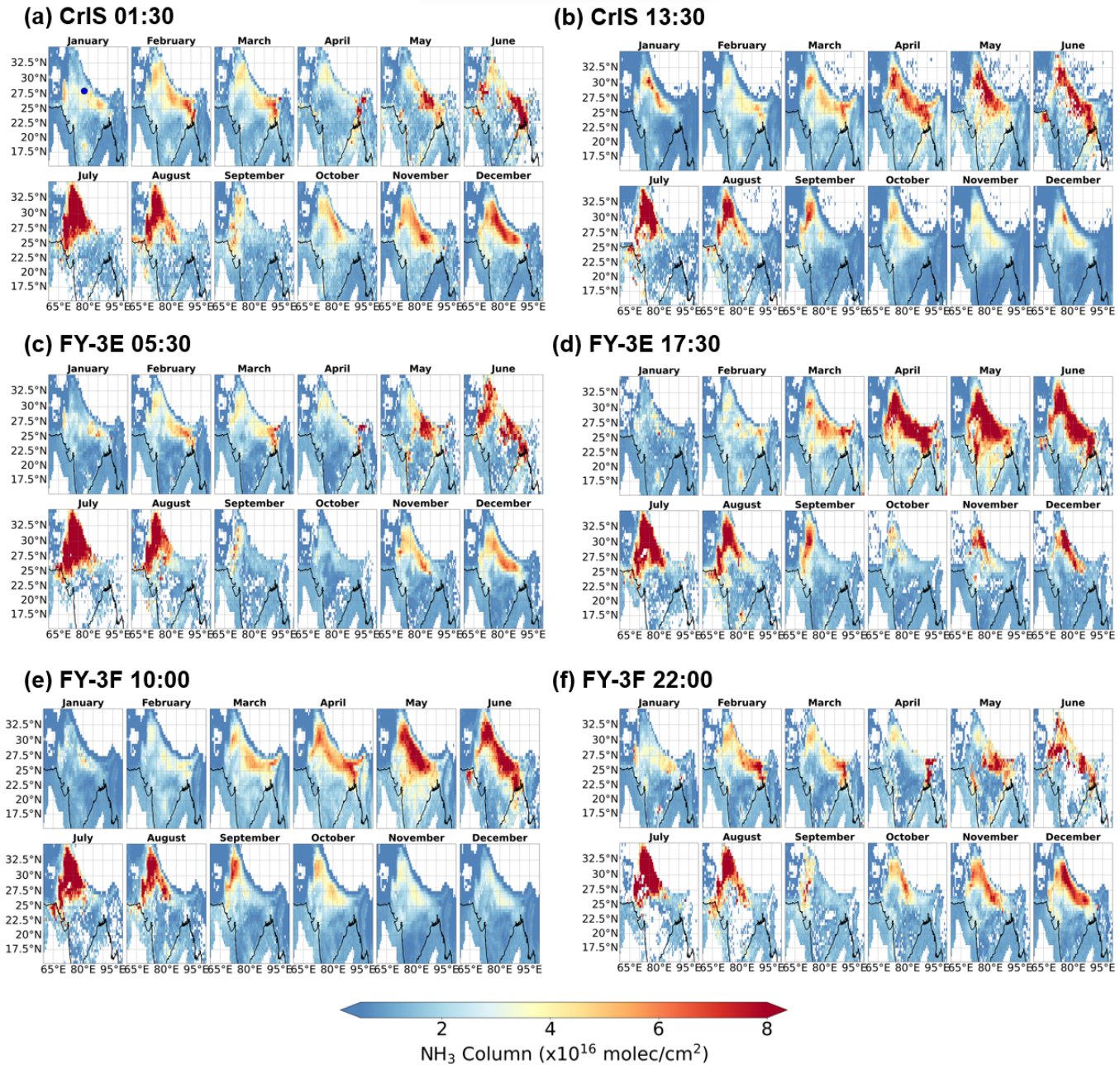

275 **Figure 6. Same as Fig. 5, but for the Indo-Gangetic Plain. The blue circle in the January panel of Fig. 6a indicates the location of the site (78°E, 38°N) analyzed in Figs. 4 and 8.**

https://doi.org/10.5194/egusphere-2026-746
Preprint. Discussion started: 16 February 2026

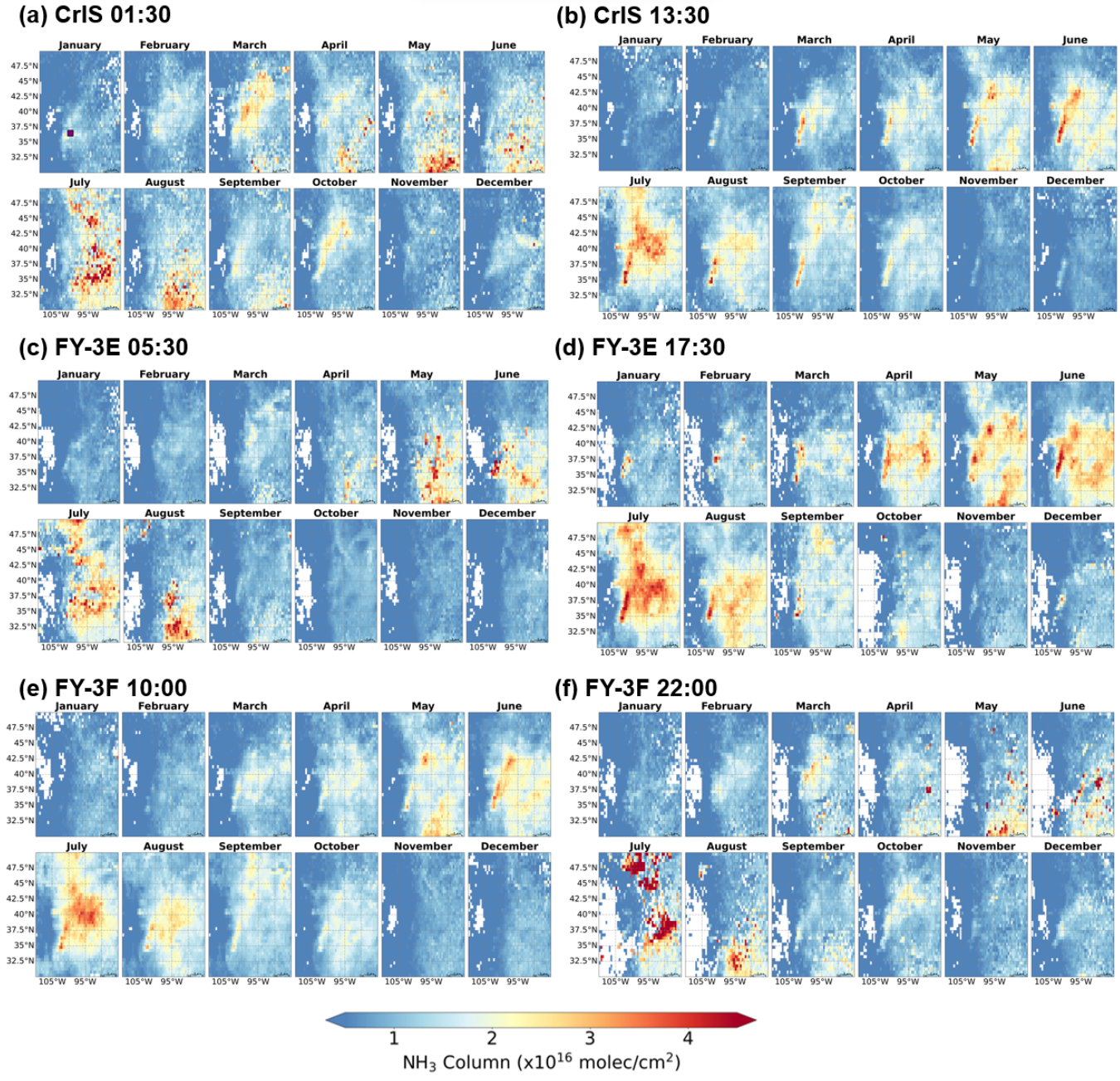

Figure 7. Same as Fig. 5, but for Central U.S.. The purple square in the January panel of Fig. 7a indicates the location of the site (100.5°W, 36.5°N) analyzed in Figs. 4 and 8.

https://doi.org/10.5194/egusphere-2026-746
Preprint. Discussion started: 16 February 2026

3.3 Comparisons with geostationary NH_3 observations from FY-4B/GIIRS

To validate the consistency of NH_3 column retrievals from polar-orbiting satellites, we perform a spatiotemporally collocated comparison between FY-3E/HIRAS-II, FY-3F/HIRAS-II and CrIS (across different diurnal periods) and the geostationary FY-4B/GIIRS, respectively. FY-3E exhibits a correlation coefficient (R) range of 0.77–0.9, FY-3F an R range of 0.68–0.9 and CrIS an R range of 0.59–0.84. As expected, daytime retrievals with larger TC show higher R than nighttime. Overall, the linear fitting lines for all polar-orbiting sensors are close to the 1:1 equivalence line against FY-4B/GIIRS retrievals, indicating generally good consistency between the polar-orbiting and geostationary satellite observations.

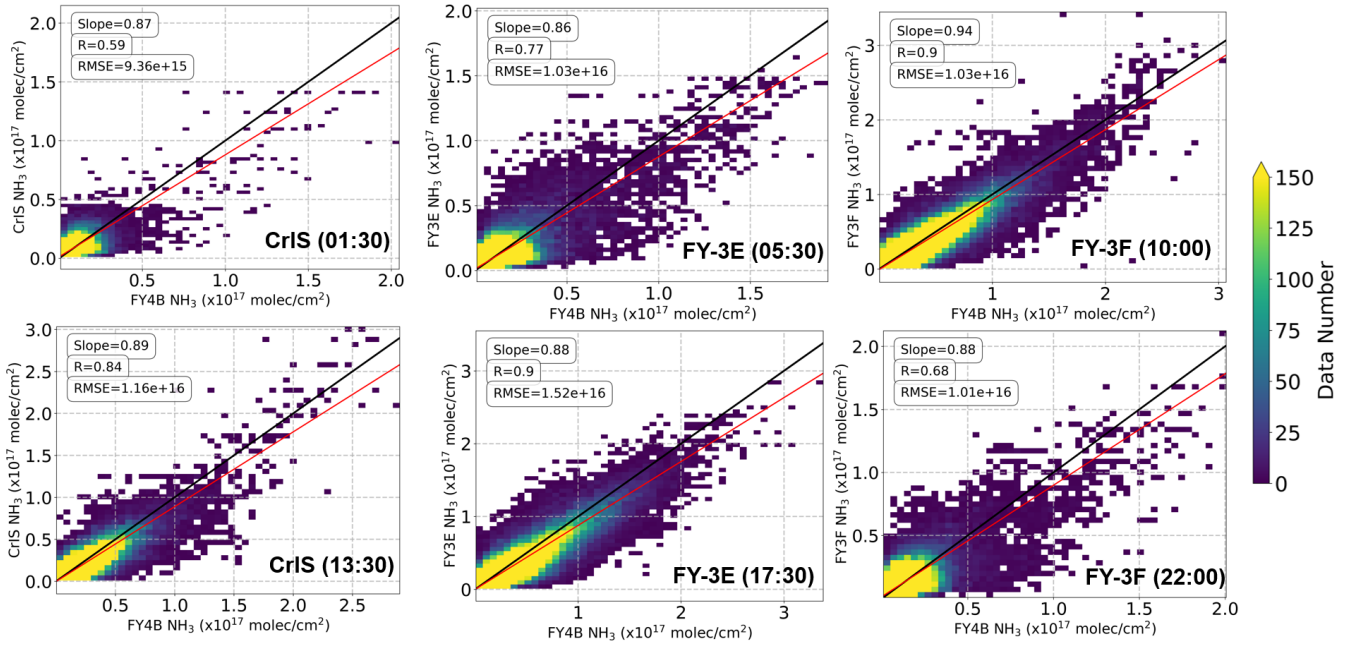

Figure 8. Comparisons of NH_3 column between polar-orbiting satellites (FY-3E/HIRAS-II, FY-3F/HIRAS-II and CrIS) retrievals and geostationary satellite (FY-4B/GIIRS) retrievals over the Indo-Gangetic Plain (75°E-95°E, 15°N-35°N) and the North China Plain (110°E-130°E, 25°N-45°N) at different times of the day in 2024. Observations are collocated when the differences in longitude and latitude are both less than 0.5° and observation time is less than 0.5 hours. The black dashed line represents the 1:1 equivalence line, with the red line indicating the linear fit. The fit's slope, correlation coefficient (R), and root mean square error (RMSE) are also provided.

3.4 Diurnal variations of the surface AVK, the retrieval uncertainty and the TC

Fig. 9 present the diurnal and seasonal dynamics of surface AVK, TC, and column retrieval uncertainty across three representative hotspots, locating in the North China Plain (118°E, 37°N), India (78°E, 28°N), and the Central U.S. (100.5°W, 36.5°N). Derived from FY-3E, FY-3F, and CrIS observations within 2.5° × 2.5° grids, the data reflect monthly averages for four key seasons (January, April, July, and October) across six daily overpass times.

https://doi.org/10.5194/egusphere-2026-746
Preprint. Discussion started: 16 February 2026

TC exhibits a consistent diurnal pattern across all regions. Midday overpasses (10:00–13:30 local solar time) see TC peak with positive values ranging from 5 to 12 K in warm months (April and July), while nighttime and early morning (01:30–05:30) bring near-zero or negative TC, particularly in January and October. Seasonal contrasts in TC amplitude are striking. Warm months feature fluctuations of up to 15 K in India, driven by intense solar heating, while cold months (January) show smaller variations, with TC confined to ±5 K for most overpasses.

The bottom layer value of column AVK, which quantifies the observational information content related to near-surface NH_3, tracks TC closely across all regions and seasons. Midday overpasses coincide with peak bottom layer column AVK (0.3–0.6), indicating robust sensitivity to near-surface NH_3 variations when TC is strongest. In contrast, nighttime and early morning bottom layer column AVK drops to 0.1–0.3, especially in January. India exhibits the most pronounced diurnal swings, with July midday bottom layer column AVK exceeding 0.6, while the Central U.S. maintains more moderate, stable values (0.2–0.4) across all seasons. Seasonally, bottom layer column AVK remains consistently higher in April and July relative to January and October, confirming that warm-season midday conditions offer the most useful observational constraints for NH_3 retrievals.

Column retrieval uncertainty follows an inverse relationship with both TC and surface AVK, as theoretical retrieval principles predict. Uncertainty peaks during nighttime and early morning and declines to minima during midday warm-season overpasses. This pattern arises because strong TC amplifies NH_3's spectral signature, while high surface AVK reduces ambiguity in separating NH_3 signals from atmospheric background variability. Large diurnal and seasonal swings in the Indo-Gangetic Plain reflect monsoon-driven humidity and extreme temperature gradients, whereas the Central U.S.'s temperate continental climate fosters lower, more stable uncertainty across all overpasses and seasons. January exhibits the highest overall uncertainty across all regions, driven by weak TC and low surface AVK, while April and July midday observations yield the lowest uncertainty.

https://doi.org/10.5194/egusphere-2026-746
Preprint. Discussion started: 16 February 2026

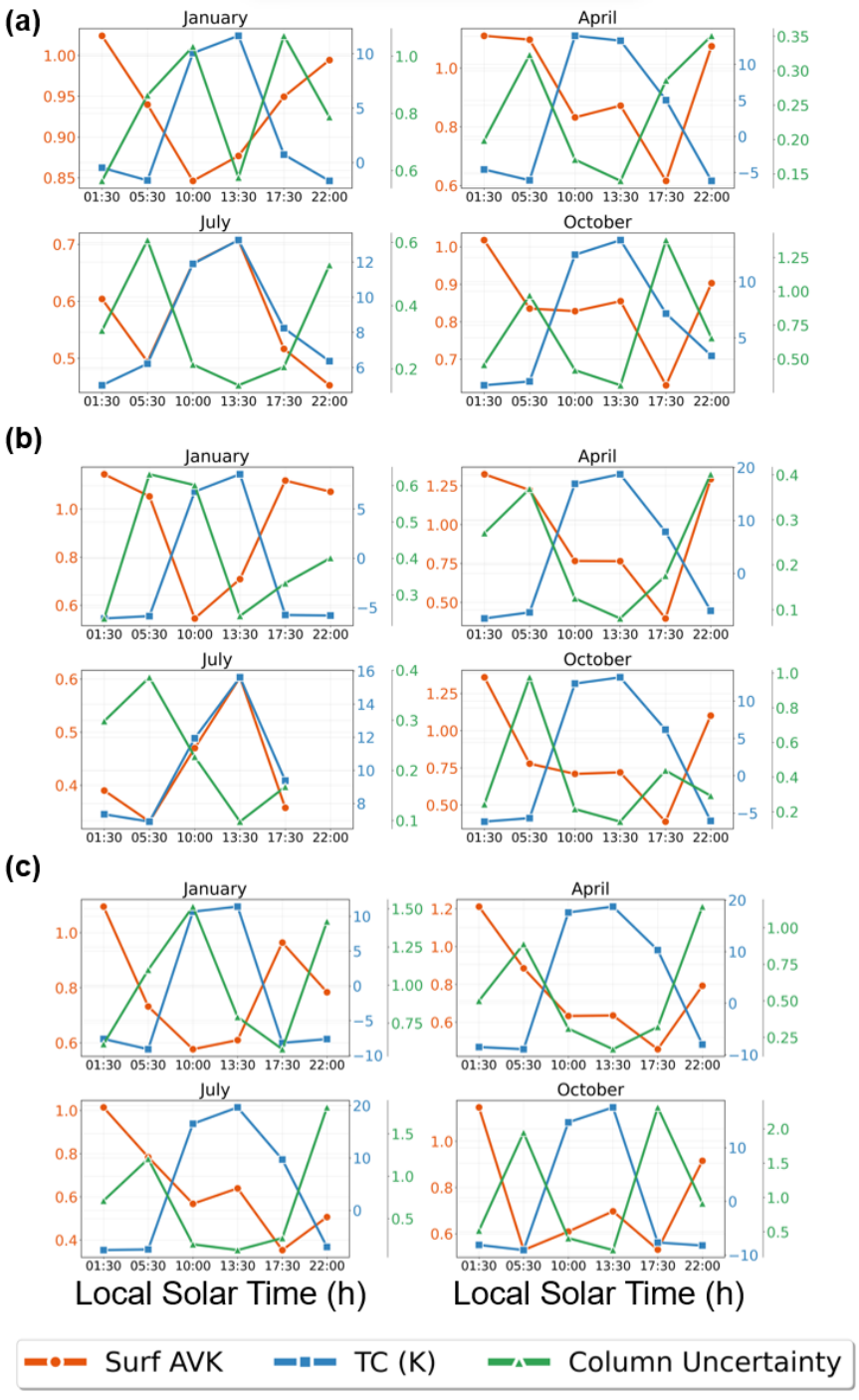

Figure 9. Diurnal cycle of surface AVK, TC and column uncertainty from FY-3E, FY-3F and CrIS over three hotspots in (a) the North China Plain (118°E, 37°N), (b) the Indo-Gangetic Plain (78°E, 28°N), and (c) Central U.S. (100.5°W, 36.5°N).

https://doi.org/10.5194/egusphere-2026-746
Preprint. Discussion started: 16 February 2026

5 Conclusions

This study develops a global monitoring framework by integrating three polar-orbiting hyperspectral infrared sounders, including FY-3E/HIRAS-II in a dawn-dusk orbit, FY-3F/HIRAS-II in a mid-morning orbit, and CrIS in an afternoon orbit. This constellation achieves quasi-geostationary-like coverage, enabling six global NH_3 column retrievals based on the optimal estimation method, for every 4-hour per day. This framework effectively captures spatial, diurnal, and seasonal dynamics of tropospheric NH_3 worldwide, with elevated columns consistently identified in major agricultural hotspots. It also validates retrieval consistency through cross-comparisons with geostationary FY-4B/GIIRS, confirming consistent spatial patterns and robust performance across different observational periods.

The NH_3 retrieval results underscore the key drivers of NH_3 variability: temperature, planetary boundary layer dynamics, and anthropogenic activities (e.g., agricultural practices) govern diurnal and seasonal cycles, while regional variations reflect differences in emission intensity and atmospheric chemistry. The constellation effectively addresses the longstanding gap of high-frequency NH_3 observations in regions lacking geostationary satellite coverage, providing a comprehensive dataset for global NH_3 cycling research. Looking forward, the upcoming integration of FY-3H/HIRAS-II launched at the end of 2025, equipped with the same HIRAS-II sensor as FY-3E and FY-3F, will homogenize the constellation, further enhancing data consistency and spatial-temporal coverage. This refined observation constellation holds great potential to advance NH_3 emission quantification, improve parameterizations in global climate and air quality models, and support evidence-based policies for anthropogenic source management.

https://doi.org/10.5194/egusphere-2026-746
Preprint. Discussion started: 16 February 2026

Appendices

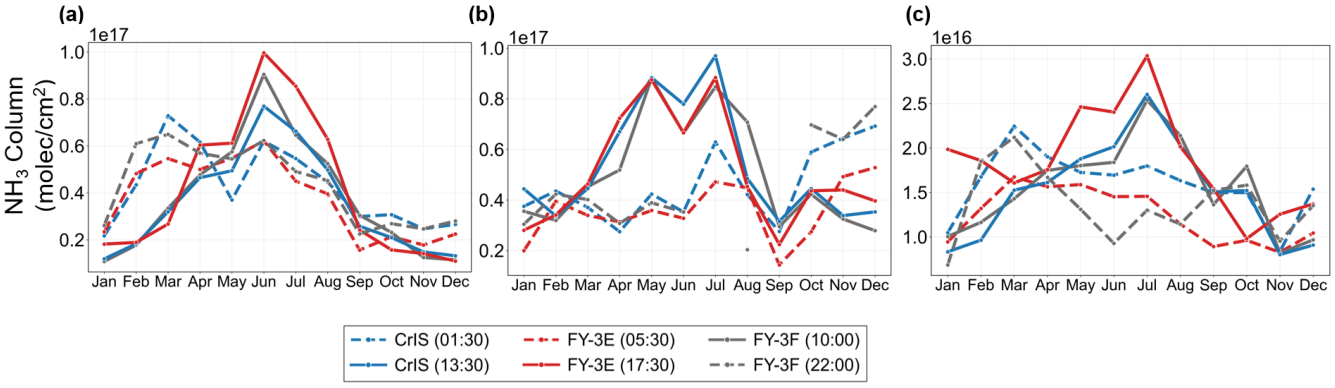

Figure A1. Seasonal variation timeseries of retrieved NH_3 total columns over (a) the North China Plain, (b) the Indo-Gangetic Plain and Central U.S.

355

Data availability

The FY-3E and FY-3F NH_3 retrieval datasets are publicly available at ZENODO (https://doi.org/10.5281/zenodo.18359451 and https://doi.org/10.5281/zenodo.18366114, respectively). Currently, the FY-3E dataset is available from January 2023 to December 2024, and the FY-3F dataset is available from January to December 2024. The GIIRS NH_3 data (from July 2022 to
360 June 2025) used in this study are publicly available on Zenodo (https://doi.org/10.5281/zenodo.17193848). Further updates on FengYun NH_3 data will be provided on the project website (https://fengyunair.github.io/). FengYun satellite Level 1 data are publicly available from the FengYun Satellite Data Center at http://satellite.nsmc.org.cn/portalsite/default.aspx. The IASI L2 ammonia satellite observations are available from the AERIS data infrastructure (https://iasi.aeris-data.fr/). The CrIS L1 spectra are publicly available from https://search.earthdata.nasa.gov/.

365 **Author contributions**

ZZ designed the experiments, and JH carried them out. ZZ and JH developed the model code and JH performed the simulations. MS and RZ assisted the satellite data pre-processing and results analysis. JH prepared the manuscript with contributions from all co-authors.

Competing interests

370 At least one of the (co-)authors is a member of the editorial board of Atmospheric Measurement Techniques.

https://doi.org/10.5194/egusphere-2026-746
Preprint. Discussion started: 16 February 2026

Acknowledgements

We gratefully acknowledge Drs. Chengli Qi, Lu Lee, Xiuqing Hu, and Feng Lu from the National Meteorological Satellite Center of China for their guidance on using the FengYun hyperspectral infrared spectra observations. We would also like to thank Drs. Cathy Clerbaux, Lieven Clarisse and Martin Van Damme for making the IASI NH_3 data publicly available.

Financial support

Z.-C. Zeng acknowledges funding from the National Natural Science Foundation of China (grant nos. 42275142, 12292981), the National Key R&D Program of China (grant no. 2022YFA1003801). This work was also supported by High-performance Computing Platform of Peking University.

https://doi.org/10.5194/egusphere-2026-746
Preprint. Discussion started: 16 February 2026

References

Abbatt, J. P. D., Benz, S., Cziczo, D. J., Kanji, Z., Lohmann, U., and Möhler, O.: Solid Ammonium Sulfate Aerosols as Ice Nuclei: A Pathway for Cirrus Cloud Formation, Science, 313, 1770–1773, https://doi.org/10.1126/science.1129726, 2006.

Adams, P. J., Seinfeld, J. H., Koch, D., Mickley, L., and Jacob, D.: General circulation model assessment of direct radiative forcing by the sulfate-nitrate-ammonium-water inorganic aerosol system, J. Geophys. Res.-Atmos., 106, 1097–1111, https://doi.org/10.1029/2000JD900512, 2001.

Bauduin, S., Clarisse, L., Theunissen, M., George, M., Hurtmans, D., Clerbaux, C., and Coheur, P.-F.: IASI's sensitivity to near-surface carbon monoxide (CO): Theoretical analyses and retrievals on test cases, J. Quant. Spectrosc. Radiat. Transf., 189, 428–440, https://doi.org/10.1016/j.jqsrt.2016.12.022, 2017.

Beer, R., Shephard, M. W., Kulawik, S. S., Clough, S. A., Eldering, A., Bowman, K. W., Sander, S. P., Fisher, B. M., Payne, V. H., Luo, M., Osterman, G. B., and Worden, J. R.: First satellite observations of lower tropospheric ammonia and methanol, Geophys. Res. Lett., 35, 2008GL033642, https://doi.org/10.1029/2008GL033642, 2008.

Behera, S. N., Sharma, M., Aneja, V. P., and Balasubramanian, R.: Ammonia in the atmosphere: a review on emission sources, atmospheric chemistry and deposition on terrestrial bodies, Environ. Sci. Pollut. Res., 20, 8092–8131, https://doi.org/10.1007/s11356-013-2051-9, 2013.

Clarisse, L., Clerbaux, C., Dentener, F., Hurtmans, D., and Coheur, P.-F.: Global ammonia distribution derived from infrared satellite observations, Nat. Geosci., 2, 479–483, https://doi.org/10.1038/ngeo551, 2009.

Clarisse, L., Shephard, M. W., Dentener, F., Hurtmans, D., Cady-Pereira, K., Karagulian, F., Van Damme, M., Clerbaux, C., and Coheur, P.: Satellite monitoring of ammonia: A case study of the San Joaquin Valley, J. Geophys. Res.-Atmos., 115, 2009JD013291, https://doi.org/10.1029/2009JD013291, 2010.

Clarisse, L., Clerbaux, C., Franco, B., Hadji-Lazaro, J., Whitburn, S., Kopp, A. K., Hurtmans, D., and Coheur, P. -F.: A Decadal Data Set of Global Atmospheric Dust Retrieved From IASI Satellite Measurements, J. Geophys. Res.-Atmos., 124, 1618–1647, https://doi.org/10.1029/2018JD029701, 2019.

Clarisse, L., Van Damme, M., Hurtmans, D., Franco, B., Clerbaux, C., and Coheur, P.: The Diel Cycle of NH_3 Observed From the FY-4A Geostationary Interferometric Infrared Sounder (GIIRS), Geophys. Res. Lett., 48, e2021GL093010, https://doi.org/10.1029/2021GL093010, 2021.

Dammers, E., Schaap, M., Haaima, M., Palm, M., Wichink Kruit, R. J., Volten, H., Hensen, A., Swart, D., and Erisman, J. W.: Measuring atmospheric ammonia with remote sensing campaign: Part 1 – Characterisation of vertical ammonia concentration profile in the centre of The Netherlands, Atmos. Environ., 169, 97–112, https://doi.org/10.1016/j.atmosenv.2017.08.067, 2017.

De Mazière, M., Thompson, A. M., Kurylo, M. J., Wild, J. D., Bernhard, G., Blumenstock, T., Braathen, G. O., Hannigan, J. W., Lambert, J.-C., Leblanc, T., McGee, T. J., Nedoluha, G., Petropavlovskikh, I., Seckmeyer, G., Simon, P. C., Steinbrecht, W., and Strahan, S. E.: The Network for the Detection of Atmospheric Composition Change (NDACC): history, status and perspectives, Atmospheric Chem. Phys., 18, 4935–4964, https://doi.org/10.5194/acp-18-4935-2018, 2018.

Ding, J., Van Der A, R., Eskes, H., Dammers, E., Shephard, M., Wichink Kruit, R., Guevara, M., and Tarrason, L.: Ammonia emission estimates using CrIS satellite observations over Europe, Atmos. Chem. Phys., 24, 10583–10599, https://doi.org/10.5194/acp-24-10583-2024, 2024.

https://doi.org/10.5194/egusphere-2026-746
Preprint. Discussion started: 16 February 2026

Erisman, J. W., Galloway, J. N., Seitzinger, S., Bleeker, A., Dise, N. B., Petrescu, A. M. R., Leach, A. M., and De Vries, W.: Consequences of human modification of the global nitrogen cycle, Philos. Trans. R. Soc. B Biol. Sci., 368, 20130116, https://doi.org/10.1098/rstb.2013.0116, 2013.

Ernst, J. W. and Massey, H. F.: The Effects of Several Factors on Volatilization of Ammonia Formed from Urea in the Soil, Soil Sci. Soc. Am. J., 24, 87–90, https://doi.org/10.2136/sssaj1960.03615995002400020007x, 1960.

Fowler, D., Coyle, M., Skiba, U., Sutton, M. A., Cape, J. N., Reis, S., Sheppard, L. J., Jenkins, A., Grizzetti, B., Galloway, J. N., Vitousek, P., Leach, A., Bouwman, A. F., Butterbach-Bahl, K., Dentener, F., Stevenson, D., Amann, M., and Voss, M.: The global nitrogen cycle in the twenty-first century, Philos. Trans. R. Soc. B Biol. Sci., 368, 20130164, https://doi.org/10.1098/rstb.2013.0164, 2013.

Galloway, J. N., Aber, J. D., Erisman, J. W., Seitzinger, S. P., Howarth, R. W., Cowling, E. B., and Cosby, B. J.: The Nitrogen Cascade, BioScience, 53, 341, https://doi.org/10.1641/0006-3568(2003)053%5B0341:TNC%5D2.0.CO;2, 2003.

Galloway, J. N., Dentener, F. J., Capone, D. G., Boyer, E. W., Howarth, R. W., Seitzinger, S. P., Asner, G. P., Cleveland, C. C., Green, P. A., Holland, E. A., Karl, D. M., Michaels, A. F., Porter, J. H., Townsend, A. R., and Vorosmarty, C. J.: Nitrogen Cycles: Past, Present, and Future, Biogeochemistry, 70, 153–226, https://doi.org/10.1007/s10533-004-0370-0, 2004.

Guo, H., Otjes, R., Schlag, P., Kiendler-Scharr, A., Nenes, A., and Weber, R. J.: Effectiveness of ammonia reduction on control of fine particle nitrate, Atmos. Chem. Phys., 18, 12241–12256, https://doi.org/10.5194/acp-18-12241-2018, 2018.

Hempel, S., Saha, C. K., Fiedler, M., Berg, W., Hansen, C., Amon, B., and Amon, T.: Non-linear temperature dependency of ammonia and methane emissions from a naturally ventilated dairy barn, Biosyst. Eng., 145, 10–21, https://doi.org/10.1016/j.biosystemseng.2016.02.006, 2016.

Holmlund, K., J. Grandell, J. Schmetz, R. Stuhlmann, B. Bojkov, R. Munro, M. Lekouara, D. Coppens, B. Viticchie, T. August , B. Theodore, P. Watts, M. Dobber, G. Fowler, S. Bojinski, A. Schmid, K. Salonen, S. Tjemkes, D. Aminou, P. Blythe, 2021. Meteosat Third Generation (MTG): Continuation and innovation of observations from geostationary orbit. Bull. Am. Meteorol. Soc. 102, E990-E1015. https://doi.org/10.1175/BAMS-D-19-0304.1.

Hua, J., Liu, S., Qi, C., Wu, S., Lee, L., Hu, X., Zhao, X., Strong, K., Flood, V., Franco, B., Clarisse, L., Clerbaux, C., Wunch, D., Roehl, C., Wennberg, P., and Zeng, Z.-C.: Observing carbon monoxide and volatile organic compounds from Canadian wildfires in 2023 from FengYun-3E/HIRAS-II in a dawn-dusk sun-synchronous orbit, Remote Sens. Environ., 327, 114829, https://doi.org/10.1016/j.rse.2025.114829, 2025.

Isaksen, I. S. A., Granier, C., Myhre, G., Berntsen, T. K., Dalsøren, S. B., Gauss, M., Klimont, Z., Benestad, R., Bousquet, P., Collins, W., Cox, T., Eyring, V., Fowler, D., Fuzzi, S., Jöckel, P., Laj, P., Lohmann, U., Maione, M., Monks, P., Prevot, A. S. H., Raes, F., Richter, A., Rognerud, B., Schulz, M., Shindell, D., Stevenson, D. S., Storelvmo, T., Wang, W.-C., Van Weele, M., Wild, M., and Wuebbles, D.: Atmospheric composition change: Climate–Chemistry interactions, Atmos. Environ., 43, 5138–5192, https://doi.org/10.1016/j.atmosenv.2009.08.003, 2009.

Jiménez, E., Cabañas, B., and Lefebvre, G. (Eds.): Environment, Energy and Climate Change I: Environmental Chemistry of Pollutants and Wastes, Springer International Publishing, Cham, https://doi.org/10.1007/978-3-319-12907-5, 2015.

Kuang, Y., Xu, W., Lin, W., Meng, Z., Zhao, H., Ren, S., Zhang, G., Liang, L., and Xu, X.: Explosive morning growth phenomena of NH3 on the North China Plain: Causes and potential impacts on aerosol formation, Environ. Pollut., 257, 113621, https://doi.org/10.1016/j.envpol.2019.113621, 2020.

Li, Z., Sun, K., Guan, K., Wang, S., Peng, B., Clarisse, L., Van Damme, M., Coheur, P.-F., Cady-Pereira, K., Shephard, M. W., Zondlo, M., and Moore, D.: Ammonia emissions and depositions over the contiguous United States derived from IASI and CrIS using the directional derivative approach, https://doi.org/10.5194/egusphere-2025-725, 5 March 2025.

Lindaas, J., Pollack, I. B., Calahorrano, J. J., O'Dell, K., Garofalo, L. A., Pothier, M. A., Farmer, D. K., Kreidenweis, S. M., Campos, T., Flocke, F., Weinheimer, A. J., Montzka, D. D., Tyndall, G. S., Apel, E. C., Hills, A. J., Hornbrook, R. S., Palm, B. B., Peng, Q., Thornton, J. A., Permar, W., Wielgasz, C., Hu, L., Pierce, J. R., Collett, J. L., Sullivan, A. P., and Fischer, E. V.: Empirical Insights Into the Fate of Ammonia in Western U.S. Wildfire Smoke Plumes, J. Geophys. Res.-Atmos., 126, e2020JD033730, https://doi.org/10.1029/2020JD033730, 2021.

Liu, M., Huang, X., Song, Y., Xu, T., Wang, S., Wu, Z., Hu, M., Zhang, L., Zhang, Q., Pan, Y., Liu, X., and Zhu, T.: Rapid SO_2 emission reductions significantly increase tropospheric ammonia concentrations over the North China Plain, Atmos. Chem. Phys., 18, 17933–17943, https://doi.org/10.5194/acp-18-17933-2018, 2018.

Liu, X., Zhang, Y., Han, W., Tang, A., Shen, J., Cui, Z., Vitousek, P., Erisman, J. W., Goulding, K., Christie, P., Fangmeier, A., and Zhang, F.: Enhanced nitrogen deposition over China, Nature, 494, 459–462, https://doi.org/10.1038/nature11917, 2013.

Lonsdale, C. R., Hegarty, J. D., Cady-Pereira, K. E., Alvarado, M. J., Henze, D. K., Turner, M. D., Capps, S. L., Nowak, J. B., Neuman, J. A., Middlebrook, A. M., Bahreini, R., Murphy, J. G., Markovic, M. Z., VandenBoer, T. C., Russell, L. M., and Scarino, A. J.: Modeling the diurnal variability of agricultural ammonia in Bakersfield, California, during the CalNex campaign, Atmos. Chem. Phys., 17, 2721–2739, https://doi.org/10.5194/acp-17-2721-2017, 2017.

Luo, Z., Zhang, Y., Chen, W., Van Damme, M., Coheur, P.-F., and Clarisse, L.: Estimating global ammonia (NH_3) emissions based on IASI observations from 2008 to 2018, Atmos. Chem. Phys., 22, 10375–10388, https://doi.org/10.5194/acp-22-10375-2022, 2022.

Myhre, G., Samset, B. H., Schulz, M., Balkanski, Y., Bauer, S., Berntsen, T. K., Bian, H., Bellouin, N., Chin, M., Diehl, T., Easter, R. C., Feichter, J., Ghan, S. J., Hauglustaine, D., Iversen, T., Kinne, S., Kirkevåg, A., Lamarque, J.-F., Lin, G., Liu, X., Lund, M. T., Luo, G., Ma, X., Van Noije, T., Penner, J. E., Rasch, P. J., Ruiz, A., Seland, Ø., Skeie, R. B., Stier, P., Takemura, T., Tsigaridis, K., Wang, P., Wang, Z., Xu, L., Yu, H., Yu, F., Yoon, J.-H., Zhang, K., Zhang, H., and Zhou, C.: Radiative forcing of the direct aerosol effect from AeroCom Phase II simulations, Atmos. Chem. Phys., 13, 1853–1877, https://doi.org/10.5194/acp-13-1853-2013, 2013.

Perrone, D.: Groundwater Overreliance Leaves Farmers and Households High and Dry, One Earth, 2, 214–217, https://doi.org/10.1016/j.oneear.2020.03.001, 2020.

Saraswati, Sharma, S. K., and Mandal, T. K.: Five-year measurements of ambient ammonia and its relationships with other trace gases at an urban site of Delhi, India, Meteorol. Atmospheric Phys., 130, 241–257, https://doi.org/10.1007/s00703-017-0512-2, 2018.

Saylor, R. D., Edgerton, E. S., Hartsell, B. E., Baumann, K., and Hansen, D. A.: Continuous gaseous and total ammonia measurements from the southeastern aerosol research and characterization (SEARCH) study, Atmos. Environ., 44, 4994–5004, https://doi.org/10.1016/j.atmosenv.2010.07.055, 2010.

Schjoerring, J. K., Husted, S., and Mattsson, M.: Physiological parameters controlling plant–atmosphere ammonia exchange, Atmos. Environ., 32, 491–498, https://doi.org/10.1016/S1352-2310(97)00006-X, 1998.

Shephard, M. W. and Cady-Pereira, K. E.: Cross-track Infrared Sounder (CrIS) satellite observations of tropospheric ammonia, Atmos. Meas. Tech., 8, 1323–1336, https://doi.org/10.5194/amt-8-1323-2015, 2015.

https://doi.org/10.5194/egusphere-2026-746
Preprint. Discussion started: 16 February 2026

Shephard, M. W., Cady-Pereira, K. E., Luo, M., Henze, D. K., Pinder, R. W., Walker, J. T., Rinsland, C. P., Bash, J. O., Zhu, L., Payne, V. H., and Clarisse, L.: TES ammonia retrieval strategy and global observations of the spatial and seasonal variability of ammonia, Atmos. Chem. Phys., 11, 10743–10763, https://doi.org/10.5194/acp-11-10743-2011, 2011.

Shephard, M. W., Dammers, E., Cady-Pereira, K. E., Kharol, S. K., Thompson, J., Gainariu-Matz, Y., Zhang, J., McLinden, C. A., Kovachik, A., Moran, M., Bittman, S., Sioris, C. E., Griffin, D., Alvarado, M. J., Lonsdale, C., Savic-Jovcic, V., and Zheng, Q.: Ammonia measurements from space with the Cross-track Infrared Sounder: characteristics and applications, Atmos. Chem. Phys., 20, 2277–2302, https://doi.org/10.5194/acp-20-2277-2020, 2020.

Sheng, M., Zhou, R., Hua, J., Han, S., Zhang, L., Wang, W., Dang, R., Cao, H., Chen, Z., Gu, Y., Liu, M., Lee, L., Qi, C., Han, C., Shephard, M. W., Guendouz, N., Viatte, C., Clarisse, L., Van Damme, M., Clerbaux, C., and Zeng, Z.-C.: Geostationary observations of atmospheric ammonia over East Asia: spatio-temporal variations revealed by three years of FY-4B/GIIRS measurements, EGUsphere [preprint], https://doi.org/10.5194/egusphere-2025-5699, 2025.

Someya, Y., Imasu, R., Shiomi, K., and Saitoh, N.: Atmospheric ammonia retrieval from the TANSO-FTS/GOSAT thermal infrared sounder, Atmos. Meas. Tech., 13, 309–321, https://doi.org/10.5194/amt-13-309-2020, 2020.

Sutton, A. D., Burrell, A. K., Dixon, D. A., Garner, E. B., Gordon, J. C., Nakagawa, T., Ott, K. C., Robinson, J. P., and Vasiliu, M.: Regeneration of Ammonia Borane Spent Fuel by Direct Reaction with Hydrazine and Liquid Ammonia, Science, 331, 1426–1429, https://doi.org/10.1126/science.1199003, 2011.

Sutton, M. A., Reis, S., Riddick, S. N., Dragosits, U., Nemitz, E., Theobald, M. R., Tang, Y. S., Braban, C. F., Vieno, M., Dore, A. J., Mitchell, R. F., Wanless, S., Daunt, F., Fowler, D., Blackall, T. D., Milford, C., Flechard, C. R., Loubet, B., Massad, R., Cellier, P., Personne, E., Coheur, P. F., Clarisse, L., Van Damme, M., Ngadi, Y., Clerbaux, C., Skjøth, C. A., Geels, C., Hertel, O., Wichink Kruit, R. J., Pinder, R. W., Bash, J. O., Walker, J. T., Simpson, D., Horváth, L., Misselbrook, T. H., Bleeker, A., Dentener, F., and De Vries, W.: Towards a climate-dependent paradigm of ammonia emission and deposition, Philos. Trans. R. Soc. B Biol. Sci., 368, 20130166, https://doi.org/10.1098/rstb.2013.0166, 2013.

Tevlin, A. G., Li, Y., Collett, J. L., McDuffie, E. E., Fischer, E. V., and Murphy, J. G.: Tall Tower Vertical Profiles and Diurnal Trends of Ammonia in the Colorado Front Range, J. Geophys. Res.-Atmos., 122, https://doi.org/10.1002/2017JD026534, 2017.

Van Damme, M., Erisman, J. W., Clarisse, L., Dammers, E., Whitburn, S., Clerbaux, C., Dolman, A. J., and Coheur, P.-F.: Worldwide spatiotemporal atmospheric ammonia (NH_3) columns variability revealed by satellite, Geophys. Res. Lett., 42, 8660–8668, https://doi.org/10.1002/2015GL065496, 2015.

Walker, J. T., Robarge, W. P., Wu, Y., and Meyers, T. P.: Measurement of bi-directional ammonia fluxes over soybean using the modified Bowen-ratio technique, Agric. For. Meteorol., 138, 54–68, https://doi.org/10.1016/j.agrformet.2006.03.011, 2006.

Wang, Q., Zhang, Q., Ma, Z., Ge, B., Xie, C., Zhou, W., Zhao, J., Xu, W., Du, W., Fu, P., Lee, J., Nemitz, E., Cowan, N., Mullinger, N., Cheng, X., Zhou, L., Yue, S., Wang, Z., and Sun, Y.: Temporal characteristics and vertical distribution of atmospheric ammonia and ammonium in winter in Beijing, Sci. Total Environ., 681, 226–234, https://doi.org/10.1016/j.scitotenv.2019.05.137, 2019.

Wang, T., Song, Y., Xu, Z., Liu, M., Xu, T., Liao, W., Yin, L., Cai, X., Kang, L., Zhang, H., and Zhu, T.: Why is the Indo-Gangetic Plain the region with the largest NH_3 column in the globe during pre-monsoon and monsoon seasons?, Atmos. Chem. Phys., 20, 8727–8736, https://doi.org/10.5194/acp-20-8727-2020, 2020.

https://doi.org/10.5194/egusphere-2026-746
Preprint. Discussion started: 16 February 2026

Warner, J. X., Wei, Z., Strow, L. L., Dickerson, R. R., and Nowak, J. B.: The global tropospheric ammonia distribution as seen in the 13-year AIRS measurement record, Atmos. Chem. Phys., 16, 5467–5479, https://doi.org/10.5194/acp-16-5467-2016, 2016.

Warner, J. X., Dickerson, R. R., Wei, Z., Strow, L. L., Wang, Y., and Liang, Q.: Increased atmospheric ammonia over the world's major agricultural areas detected from space, Geophys. Res. Lett., 44, 2875–2884, https://doi.org/10.1002/2016GL072305, 2017.

Weber, R. J., Guo, H., Russell, A. G., and Nenes, A.: High aerosol acidity despite declining atmospheric sulfate concentrations over the past 15 years, Nat. Geosci., 9, 282–285, https://doi.org/10.1038/ngeo2665, 2016.

Wells, K. C., Millet, D. B., Payne, V. H., Deventer, M. J., Bates, K. H., De Gouw, J. A., Graus, M., Warneke, C., Wisthaler, A., and Fuentes, J. D.: Satellite isoprene retrievals constrain emissions and atmospheric oxidation, Nature, 585, 225–233, https://doi.org/10.1038/s41586-020-2664-3, 2020.

Wells, K. C., Millet, D. B., Payne, V. H., Vigouroux, C., Aquino, C. A. B., De Mazière, M., De Gouw, J. A., Graus, M., Kurosu, T., Warneke, C., and Wisthaler, A.: Next-Generation Isoprene Measurements From Space: Detecting Daily Variability at High Resolution, J. Geophys. Res.-Atmos., 127, e2021JD036181, https://doi.org/10.1029/2021JD036181, 2022.

Zavyalov, V., Esplin, M., Scott, D., Esplin, B., Bingham, G., Hoffman, E., Lietzke, C., Predina, J., Frain, R., Suwinski, L., Han, Y., Major, C., Graham, B., and Phillips, L.: Noise performance of the CrIS instrument, J. Geophys. Res.-Atmos., 118, https://doi.org/10.1002/2013JD020457, 2013.

Zeng, Z.-C.: Global carbon monoxide retrieval from the hyperspectral infrared atmospheric sounder-II onboard FengYun-3E in a dawn-dusk sun-synchronous orbit, J. Quant. Spectrosc. Radiat. Transf., 333, 109336, https://doi.org/10.1016/j.jqsrt.2024.109336, 2025.

Zeng, Z.-C., Lee, L., Qi, C., Clarisse, L., and Van Damme, M.: Optimal estimation retrieval of tropospheric ammonia from the Geostationary Interferometric Infrared Sounder on board FengYun-4B, Atmos. Meas. Tech., 16, 3693–3713, https://doi.org/10.5194/amt-16-3693-2023, 2023.

Zeng, Z.-C., Clarisse, L., Franco, B., Clerbaux, C., Theys, N., Qi, C., Lee, L., Zhu, L., Hu, X., Gu, M., and Zhang, P.: Volcanic sulfur dioxide monitored from a constellation of FengYun hyperspectral infrared sounders in dawn-dusk, mid-morning, and afternoon sun-synchronous orbits, Remote Sens. Environ., 331, 115057, https://doi.org/10.1016/j.rse.2025.115057, 2025.

Zhan, X., Adalibieke, W., Cui, X., Winiwarter, W., Reis, S., Zhang, L., Bai, Z., Wang, Q., Huang, W., and Zhou, F.: Improved Estimates of Ammonia Emissions from Global Croplands, Environ. Sci. Technol., 55, 1329–1338, https://doi.org/10.1021/acs.est.0c05149, 2021.

Zhang, C., Qi, C., Yang, T., Gu, M., Zhang, P., Lee, L., Xie, M., and Hu, X.: Evaluation of FY-3E/HIRAS-II Radiometric Calibration Accuracy Based on OMB Analysis, Remote Sens., 14, 3222, https://doi.org/10.3390/rs14133222, 2022a.

Zhang, L., Chen, Y., Zhao, Y., Henze, D. K., Zhu, L., Song, Y., Paulot, F., Liu, X., Pan, Y., Lin, Y., and Huang, B.: Agricultural ammonia emissions in China: reconciling bottom-up and top-down estimates, Atmos. Chem. Phys., 18, 339–355, https://doi.org/10.5194/acp-18-339-2018, 2018.

Zhang, P., Hu, X., Lu, Q., Zhu, A., Lin, M., Sun, L., Chen, L., and Xu, N.: FY-3E: The First Operational Meteorological Satellite Mission in an Early Morning Orbit, Adv. Atmos. Sci., 39, 1–8, https://doi.org/10.1007/s00376-021-1304-7, 2022b.

https://doi.org/10.5194/egusphere-2026-746
Preprint. Discussion started: 16 February 2026

Zhang, P., Hu, X., Sun, L., Xu, N., Chen, L., Zhu, A., Lin, M., Lu, Q., Yang, Z., Yang, J., and Wang, J.: The On-Orbit Performance of FY-3E in an Early Morning Orbit, Bull. Am. Meteorol. Soc., 105, E144–E175, https://doi.org/10.1175/BAMS-D-22-0045.1, 2024.

Zhang, Y., Dore, A. J., Ma, L., Liu, X. J., Ma, W. Q., Cape, J. N., and Zhang, F. S.: Agricultural ammonia emissions inventory and spatial distribution in the North China Plain, Environ. Pollut., 158, 490–501, https://doi.org/10.1016/j.envpol.2009.08.033, 2010.

Zhou, M., Deng, Z., Robert, C., Zhang, X., Zhang, L., Wang, Y., Qi, C., Wang, P., and Mazière, M. D.: The First Global Map of Atmospheric Ammonia (NH_3) as Observed by the HIRAS/FY-3D Satellite, Adv. Atmospheric Sci., 41, 379–390, https://doi.org/10.1007/s00376-023-3059-9, 2024.